Phase diagrams of liquid-phase mixing in multi-component metal-organic framework glasses constructed by quantitative elemental nano-tomography

Sean M. Collins,[1,a,b)] Katherine E. MacArthur,[2,a,b)] Louis Longley,[1] Robert Tovey,[3] Martin Benning,[4] Carola-Bibiane Schönlieb,[3] Thomas D. Bennett[1] and Paul A. Midgley[1]

[1]*Department of Materials Science and Metallurgy, University of Cambridge, 27 Charles Babbage Road, Cambridge CB3 0FS, United Kingdom*

[2]*Ernst Ruska-Centre for Microscopy and Spectroscopy with Electrons and Peter Grünberg Institute, Forschungszentrum Jülich, 52425 Jülich, Germany*

[3]*Centre for Mathematical Sciences, University of Cambridge, Wilberforce Road, Cambridge CB3 0WA, United Kingdom*

[4]*School of Mathematical Sciences, Queen Mary University of London, Mile End Road, London E1 4NS, United Kingdom*

Several distinct mixing processes and resulting microstructures have recently been reported in multicomponent glasses prepared from multiple metal-organic frameworks (MOFs). Here, two illustrative examples of multicomponent zeolitic imidazolate framework (ZIF) glasses, the $(a_T\text{ZIF-4-Co})_{0.5}(a_g\text{ZIF-62})_{0.5}$ blend and the $a_g[(\text{ZIF-67})_{0.2}(\text{ZIF-62})_{0.8}]$ flux melted glass, are studied. These materials are characterized by quantitative X-ray energy dispersive spectroscopy in the scanning transmission electron microscope (STEM). By advancing a partial ionization cross-section methodology using standards of arbitrary morphology, quantitative nanoscale elemental analysis throughout the glass volume is achieved. In turn, phase diagrams describing the mixing states are presented, offering mechanistic insight into the formation of the observed microstructures. Significant miscibility was observed in $a_g[(\text{ZIF-67})_{0.2}(\text{ZIF-62})_{0.8}]$. These findings establish phase-segregation and inter-diffusion as two processes in multi-component glass formation, which explains the different outcomes observed in blending and flux-melting.

[a)]Sean M. Collins and Katherine E. MacArthur contributed equally to this work.
[b)]Authors to whom correspondence should be addressed. Electronic mail: smc204@cam.ac.uk, k.macarthur@fz-juelich.de

I. Introduction

Glasses comprised of two or more materials are produced through a variety of mixing processes. Inorganic glasses may be prepared through flux melting,[1] where a low melting temperature (T_m) of one component is used to facilitate early-onset melting of a second component with a significantly higher T_m. Block organic copolymers may be blended together – though could exhibit de-mixing and phase separation,[2] and bulk metallic glasses may be produced through liquid-phase alloying.[3] Many of these mixing processes are observed across the range of traditional glass materials. The resulting structures are largely governed by the miscibility and viscosities of the glass components in the liquid phase.[1] It is not clear which of these mixing processes or other alternatives determines blend formation in the emerging family of metal-organic framework (MOF) glasses.[4]

Initial reports on the preparation of multicomponent MOF glasses suggest that two cases may arise from the combination of different MOF domains within the same glass material. The first occurs when two MOF structures are heated together above their respective T_ms. Upon cooling to room temperature, a blend is formed in which MOF domains are interlocked together.[5] The second (flux melting) involves use of one liquid MOF as a high temperature solvent for one which does not possess an accessible T_m.[6] The potential outcomes can therefore, in theory, be selected based on the melting temperatures and viscosities of the constituent phases, though the prediction of products is complicated by the temperature dependence of the viscosities. However, existing measurements do not resolve the local details of composition and material density that accurately describe the phase space of mixing in these materials. Electron microscopy has been applied to reveal domain structure,[5] but quantitative analysis of the composition of nanoscale volumes is required to address open questions underpinning the fundamental mixing processes used in their preparation.

Here, we examine two mixing processes in multicomponent zeolitic imidazolate framework (ZIF) glasses using quantitative analytical electron tomography. ZIFs are a subcategory of MOFs, in which tetrahedral metal nodes are connected by imidazolate-based organic ligands into three-dimensional frameworks.[7] Several members of this family melt at ca 450 C, and the liquids can be quenched to hybrid analogues of silica glass.[8] Combined scanning transmission electron microscopy (STEM) and X-ray energy dispersive spectroscopy (EDS) in a tilt-series tomography scheme enables three-dimensional chemical imaging and simultaneous quantification of composition and material density throughout the volume of a material. Importantly, this now enables the construction of experimental phase diagrams for mixing in multicomponent melt-quenched MOF-glasses. The results presented here, for a blend of Co ZIF-4 and ZIF-62, termed $(a_T\text{ZIF-4-Co})_{0.5}(a_g\text{ZIF-62})_{0.5}$, and for flux melting of ZIF-67 and ZIF-62, termed $a_g[(\text{ZIF-67})_{0.2}(\text{ZIF-62})_{0.8}]$, where a_g and a_T indicate melt quenched glass and thermally amorphized phases, respectively, begin to establish differences in the miscibility of mixed ZIF glasses.

STEM-EDS tomography has been applied to a variety of materials science imaging problems from binary alloy[9,10] and composite[11] metal nanoparticles to complex metallurgical samples[12–14] as well as organic/inorganic composite materials.[15] In the majority of cases, the reconstructions are qualitative or make use of quantification methods without calibration standards ('standardless' quantification). The Cliff-Lorimer or 'k-factor' approach,[16] for example, often uses calculated coefficients with associated errors of ~10% or more.[17] STEM-EDS tomography with standards-based quantification, such as tomography incorporating the ζ-factor method with pure element standards,[17] has been applied in noble metal alloy nanoparticles[18,19] and in semiconductor nanostructures.[20] An alternative framing in terms of partial ionization cross-sections, equivalent to the ζ-factor method, enables for direct comparison of imaging and spectroscopic signals in STEM.[21] The partial ionization cross-section is particularly beneficial for the study of nanomaterials as it directly determines the number of atoms per unit of illumination area in the

spectrum image,[22] the 'data-cube' consisting of spectra recorded at each spatial position in the image. In this work, we combine these standards-based cross-sections for quantitative STEM-EDS with advanced electron tomographic reconstruction techniques to gain insight into the glass formation processes in ZIF blending, and flux melting processes, at the nanoscale and throughout their three-dimensional volume.

Whereas previous approaches to standards-based STEM-EDS approaches have relied on single element samples in wedge[21] or needle[23] geometries or on tomography of approximately spherical particle geometries,[24] the method presented here use electron tomography of single-element standards with arbitrary sample geometry to determine partial ionization cross-sections for characteristic X-ray emission. This approach to the retrieval of useful calibration information relies on high-quality tomographic reconstructions, made possible through total-variation (TV) regularized reconstruction algorithms,[25] a variant of compressed sensing electron tomography.[26] In our implementation, the TV-norm used in the regularized tomography algorithm is applied in all three dimensions of the reconstruction volume.[14,27] Moreover, a second-order total-variation ('TV^2')[28,29] regularization term is introduced for 3D STEM-EDS to enable high quality compressed sensing tomographic reconstructions from only 15 projections while also allowing for gradients in the chemical composition. The piece-wise constant character of homogeneous solids motivates use of the TV-norm to recover particle morphology and thickness from ADF-STEM data. Contrastingly, in the case of variation of 3D composition we expect STEM-EDS data to be better explained by a piece-wise linear reconstruction, encouraging the use of the TV^2-norm for STEM-EDS tomography of MOF glasses where solvation and diffusion across phases is possible during the heat treatments used in preparing the materials. TV^2 regularization promotes sparsity in the second-order gradient domain, allowing piece-wise linear solutions with sharp interfaces. In a discretized domain, due to the finite difference approximation, these interfaces may only be blurred up to an order of a few pixels wide. Alternatives incorporating both first and second order

contributions exist,[5,30] but were overly susceptible to fitting to noise for these dose-controlled, quantitative EDS tomography experiments.

Here, advances in STEM-EDS quantification and tomography are applied to key examples of metal-organic framework blends and flux melted glasses. These results establish the mixing processes in these new classes of MOF materials with 3D nanoscale precision. This progress grounds hypotheses on the glass formation routes in these systems, which may prove transferable to other MOF glasses. Importantly, an understanding of the mixing processes establishes guiding principles for selecting desired blending, or flux-melting outcomes and for exerting control over the mechanical, and chemical, functionalities of these emerging, complex amorphous materials.

II. Results and discussion

A. Determination of X-ray EDS cross-sections

A general method for the determination of STEM-EDS cross-sections was developed for arbitrary particle geometries by using TV-regularized ADF-STEM tomography and STEM-EDS of calibration standards. In this case, Co ZIF-4 ($Co(Im)_2$, Im: imidazolate, $C_3H_3N_2^-$) and ZIF-62 ($Zn(Im)_{1.75}(bIm)_{0.25}$, bIm: benzimidazolate, $C_7H_5N_2^-$) crystalline precursor particles were selected as calibration standards with similar composition and density to the ZIF glasses targeted for quantitative STEM-EDS tomography. Calibrations were carried out on two analytical electron microscopes: an FEI Osiris microscope at the University of Cambridge ('Cambridge Osiris') and an FEI Titan microscope at the Ernst-Ruska Centre ('ER-C Titan'), both fitted with the 'Super-X' quadrant detector geometry. This approach enabled validation of the methodology and for highlighting holder and column-specific calibration requirements. First, STEM-EDS maps were acquired at zero tilt followed by acquisition of an ADF-STEM tilt-series. Each particle selected for calibration was in the centre of a grid square in order to maximise tilt range for the ADF

tomography and minimise shadowing for the EDS.[31] Additional details are given in the Supplementary Material. Due to some initial volume reduction of the particles observed in STEM consistent with amorphization under the electron beam, the standards were assigned the pycnometric densities of the amorphous Co ZIF-4 and amorphous ZIF-62 phases, approximately 1.56 g cm^{-3}, and the composition as expected from their stoichiometry.[5,6] After the initial contraction, the particles were stable under the electron beam and showed no further morphological changes. This electron beam damage was observed for all ZIF-based samples studied here, and all measurements were taken from particles in the stable response regime after initial electron beam damage, providing a consistent baseline for the application of calibrations. The atomic density for the Co atoms in ZIF-4 precursors was therefore taken as 4.87 atoms nm^{-3} and the atomic density for Zn atoms in ZIF-62 was taken as 4.45 atoms nm^{-3}, as determined from the pycnometric density and stoichiometry of the crystal.

For a known reference atomic density, known experimental parameters (i.e. electron beam current, pixel size, dwell time), and known sample thickness, it is possible to determine partial cross-sections for the EDS detectors on a particular microscope operated with a particular sample holder and accelerating voltage.[21] The detector response varies with holder as well as with sample position in the column and sample tilt due to shadowing of one or more detectors.[31,32] Here, these differences were minimised by fixing the tilt angle to zero (negligible shadowing condition[31]) for the measurement and application of partial cross-sections and operating a consistent lens setting to determine the focal plane and the sample position. Additionally, the sample geometry was consistent throughout with the grid bars below the support film which was below the sample material (with the detectors above this assembly). The live time was taken from the tags in the Esprit software from Bruker used for EDS data acquisition and the beam current was measured using the electron energy loss spectrometer drift tube. Finally, the experimental pixel size was selected to be slightly smaller than the beam diameter such that an oversampling regime occurred

and the illumination area could be approximated to pixel area. Subsequent binning of the spectrum image was applied during post processing in order to achieve sufficient signal-to-noise in individual spectra and ensure accurate extraction of net X-ray counts.

TV-regularized ADF-STEM tomography yielded thickness information for calibration samples of arbitrary geometry. Figure 1 presents ADF-STEM micrographs, tomographic reconstructions of the ZIF particle volume, and thickness maps determined from the tomographic reconstruction for four particles used as standards on the Cambridge Osiris microscope (two particles for each Co and Zn). Figure S5 presents the corresponding data for particles used as calibration standards on the ER-C Titan microscope. In order to systematically determine thickness and to minimize bias from subjective parameter selection, it was necessary to segment the ADF-STEM tomographic reconstructions in an automated way. Previous reports have suggested an edge spread function (ESF) fitting as an approach for automated threshold selection[19,24] (see also Supplementary Material). Briefly, the ESF is used to fit the intensity profile from within the particle volume to the vacuum or support material outside. The ESF fit then returns the threshold value at the maximum gradient in this profile. However, previous methods have used multiple single line profiles through the volume of approximately spherical particles.[24] An approximately spherical morphology is necessary to use such an approach in a straightforward way given the line profile must traverse the particle surface at an approximately normal orientation which may not be easily identified in an arbitrary geometry for a single line profile. Instead, for the ZIF particles here, a modified approach was taken to the ESF fitting method. Rather than individual line profiles, a global parameter of the particle was sought in terms of the particle volume. For a series of threshold values, the measured particle volume was calculated. Then, finite differences in the volume between adjacent threshold values yielded the global parameter ΔV, the differential particle volume. Plotting ΔV against the thresholds resulted in a sigmoid curve appropriate for ESF fitting (see also Supplementary Material). The three-dimensional particle surfaces presented

in Figure 1 show the segmentation results for the Cambridge Osiris standards. Finally, the thickness was determined from projection (summation) of the binarized volume obtained from the segmentation step along the electron beam direction.

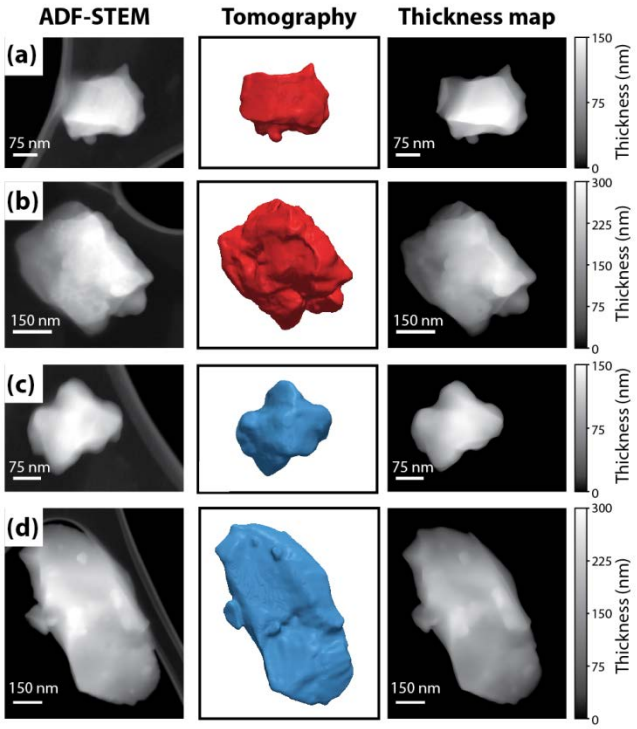

Fig. 1. Crystalline MOF particles used as calibration standards for determination of EDS cross-sections on the Cambridge Osiris microscope at 80 kV. An ADF-STEM micrograph, a surface rendering of the segmented tomographic reconstruction, and the corresponding thickness map are shown (a)-(b) crystalline Co ZIF-4 particles and (c)-(d) crystalline ZIF-62 particles.

The thickness maps replicate the features in the ADF-STEM images, but with the amorphous carbon support film removed. A few small errors in the particle segmentation at edges and interfaces with thick regions of the amorphous carbon film were observed, but these were negligible in the context of the number of pixels in the entire thickness maps. The removal of the additional thickness from the carbon support film is essential for determining the thickness of the sample contributing to the Zn or Co EDS signal only. Moreover, the ADF-STEM micrographs show intensities which are not calibrated. The spatial dimension (pixel size) is calibrated and this

calibration applies to the reconstructed volume (volume elements or voxels). The thickness maps are therefore determined on an absolute scale in nm.

Next, the thickness map information was combined with the reference atomic density and experimental parameters according to the formula:

$$I_A = \left(\frac{\rho_{A,ref}\tau i}{e}\right)\sigma_A t \qquad (1)$$

where I_A is the recorded intensity for species A in counts, $\rho_{A,ref}$ is the reference atomic density, τ is the dwell time in s, i is the electron beam current, e is the elementary charge, σ_A is the cross-section in barns (b), and t is the thickness in nm. This formula enables the construction of a plot of recorded intensity as a function of thickness, which varies linearly with the cross-section. The thickness map data included a variety of particle thicknesses, providing the necessary input for a linear fit to determine the cross-sections for the K_α and K_β X-ray emission lines for Co and Zn. C and N *K* lines were not analyzed due to the presence of the carbon film, poor background modelling at low energies, and the possibility of enhanced absorption effects. Absolute quantification of the Co and Zn composition requires Co and Zn X-ray lines only. Figure 2 presents example fits for the Cambridge Osiris data-sets. Figure S6 presents the fitting data for the ER-C Titan data-sets. In each case, data from two particles were combined for the determination of the cross-section from different areas of the sample grid. The match in the linear response provides improved confidence that the particles are representative of the ensemble composition of the precursor material as well as confidence in the automated thresholding method. Moreover, the linear response to >250 nm thickness provided strong evidence that the EDS signal in these samples was monotonic and linear as a function of thickness, satisfying the projection requirement for tomographic reconstruction and the linearity assumption for the EDS quantification. The linear response showed no evidence of significant X-ray absorption in the

samples. EDS signals on the corresponding mixed-phase ZIF glass blend samples were therefore considered suitable for quantitative STEM-EDS tomography.

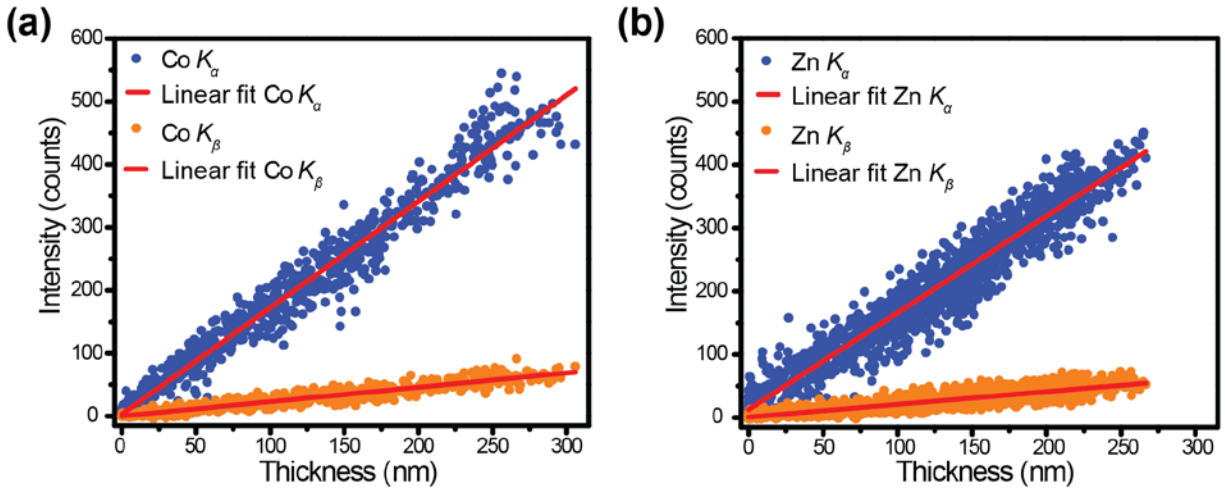

Fig. 2. Determination of (a) Co and (b) Zn cross-sections from electron tomography of ZIF crystalline precursor standards shown in Figure 1, including data from both particles for each element which are coincident using thickness data from systematically segmented reconstructions.

Table I presents the measured cross-sections for both microscopes. These measured cross-sections were of similar magnitude to those measured previously on other similar microscope and detector systems using pure element metallic standards,[21] suggesting a degree of universality to the cross-sections invariant with the selected reference. These values also provide supporting evidence that the reference densities were appropriate. Some variation between the microscopes was observed, particularly in the Co cross-sections, as expected for differences in detector shadowing[32] due to differences in the geometry of the Osiris and Titan electron optical columns.[33] There are notable differences in the column and pole piece configuration between the Osiris (Tecnai) platform and the Titan column. The cross-sections are partial cross-sections in the sense that the detectors cover a highly limited solid angle (approximately 0.7 sr).

Table I. Cross-sections determined from ZIF standards for Co and Zn K lines, obtained using Fischione tomography holders at 0° tilt and with an accelerating voltage of 80 kV.

	Cambridge Osiris (b)	ER-C Titan (b)
Co K_α	3.38	2.70
Co K_β	0.45	0.36
Zn K_α	2.48	2.51
Zn K_β	0.32	0.30

B. Quantitative STEM-EDS tomography

The instrument- and voltage-specific calibrations were applied to the two systems observed to date when preparing glasses from two separate MOF components. Comprehensive bulk characterization of $(a_T$ZIF-4-Co$)_{0.5}(a_g$ZIF-62$)_{0.5}$ and a_g[(ZIF-67$)_{0.2}$(ZIF-62$)_{0.8}$] materials has been reported previously and is not reproduced here.[5,6] The first sample, examined on the Cambridge Osiris microscope, was a $(a_T$ZIF-4-Co$)_{0.5}(a_g$ZIF-62$)_{0.5}$ glass blend.[5] This ZIF glass blend has been reported to exhibit predominantly heterogeneous mixing, with minimal diffusion at the interfaces attributed to the high viscosities of the constituent phases at the temperatures used to prepare the glass blend. Figure 3 presents two-dimensional EDS mapping and EDS tomography results for a particle of this $(a_T$ZIF-4-Co$)_{0.5}(a_g$ZIF-62$)_{0.5}$ blend. The EDS map highlights that the particle consisted of an upper Zn-rich domain and a lower Co-rich domain (Figure 3), consistent with the domain structure in previous reports.[5] Additionally, Figure 3 presents a reprojection of the EDS tomography volume as well as two orthogonal planes cut through the volume, termed 'orthoslices' (labeled *xy* for the plan view orientation of the particle and *xz* for the cross-sectional view in/out of the page in the EDS map shown). In each of these visualizations, the intensities of the Co and Zn colormaps are scaled identically (black set to zero, identical maximum intensities)

in terms of the number of Co and Zn atoms in each pixel (reprojection) or voxel (orthoslices). The *xz* orthoslice highlights the interface region. There is a very narrow region shaded in purple indicating Co and Zn co-located in pixels at the interface. However, this region is narrow in the three-dimensional volume with single-phase regions immediately on either side (indicated by arrows in Figure 3). Due to the orientation of the interface, it is not possible to directly infer an interface width from the orthoslice because the interface is inclined relative to the coordinate system of the microscope.

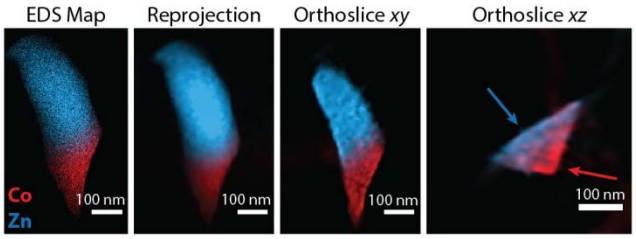

Fig. 3. Visualization of the quantitative STEM-EDS reconstruction of $(a_T\text{ZIF-4-Co})_{0.5}(a_g\text{ZIF-62})_{0.5}$. The reprojection of the reconstruction is compared with the EDS map for reference as well as two orthogonal slices through the reconstruction volume. In the *xz* orthoslice, red and blue arrows indicate single-metal Co (red) and Zn (blue) regions on either side of an interface. The color intensity is proportional to the number of atoms (same scale for each element).

A particle from a second system was examined on the ER-C Titan. This material, $a_g[(\text{ZIF-67})_{0.2}(\text{ZIF-62})_{0.8}]$ is formed from a flux-melting process, in which the Co phase (ZIF-67, $Co(mIm)_2$, mIm: 2-methylimidazolate, $C_4H_5N_2^-$) undergoes melting in the presence of the high temperature liquid ZIF-62.[6] ZIF-67 on its own does not exhibit melting below its decomposition temperature at approximately 510 °C.[6] Cooling of the liquid formed at 497 °C (above the melting temperature of ZIF-62 and below the decomposition temperature of ZIF-67), however, produced a fully amorphous solid.[6] Characterization of the resulting flux-melted glass revealed diffuse interfaces in two-dimensional STEM-EDS mapping.[6]

Figure 4 presents a two-dimensional STEM-EDS map and visualization of the quantitative STEM-EDS tomographic reconstruction. In this particle, the domain structure of the Zn-rich and

Co-rich was not clear in two-dimensional mapping, showing the expected diffuse boundaries as in previous reports.[6] The orthoslices highlight further detail, depicting substantial volumes of the particle with purple intensity, intermediate to the red and blue color scales of the Co and Zn. The *xz* orthoslice, moreover, shows that there is a relatively phase-pure Zn (blue) region visible in cross-section which is attached to a band of purple intensity, suggesting remnant single-phase ZIF-62 and predominantly mixed ZIF-62 and ZIF-67 in the Co-containing domains. The absolute quantification scaling in these reconstructions enables the direct interpretation of these intensities, confirming homogeneous mixing of Zn and Co dominates in the Co-rich regions of the a_g[(ZIF-67)$_{0.2}$(ZIF-62)$_{0.8}$] blend.

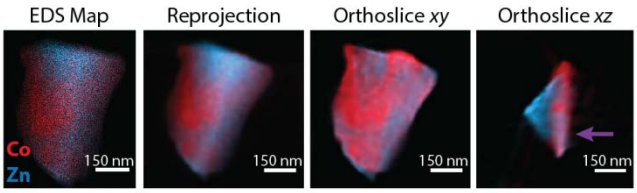

Fig. 4. Visualization of the quantitative STEM-EDS reconstruction of a_g[(ZIF-67)$_{0.2}$(ZIF-62)$_{0.8}$]. The reprojection of the reconstruction is compared with the EDS map for reference as well as two orthogonal slices through the reconstruction volume. The color intensity is proportional to the number of atoms (same scale for each element).

Figure 5 presents additional three-dimensional visualizations of the (a_TZIF-4-Co)$_{0.5}$(a_gZIF-62)$_{0.5}$ (Figure 5(a)) and the a_g[(ZIF-67)$_{0.2}$(ZIF-62)$_{0.8}$] (Figure 5(b)) blend particles. The (a_TZIF-4-Co)$_{0.5}$(a_gZIF-62)$_{0.5}$ chemical domain structure is relatively simple with two domains and a narrow interface region. In the a_g[(ZIF-67)$_{0.2}$(ZIF-62)$_{0.8}$] particle, the predominantly Zn-rich region is now more easily visualized as a ZIF-62 domain embedded in a ZIF-67 (Co) volume underneath.

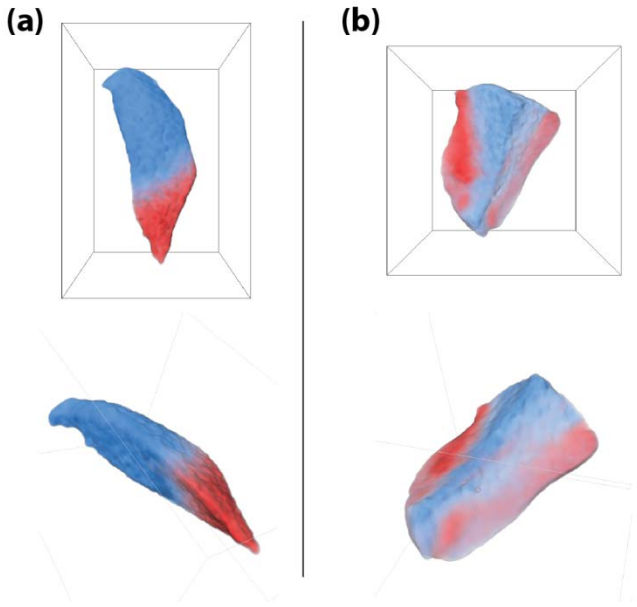

Fig. 5. Volume renderings of the elemental reconstructions for (a) $(a_T\text{ZIF-4-Co})_{0.5}(a_g\text{ZIF-62})_{0.5}$ and (b) $a_g[(\text{ZIF-67})_{0.2}(\text{ZIF-62})_{0.8}]$. The color intensity is proportional to the number of atoms (same scale for each element). Two orientations are shown to aid in the three-dimensional visualization of the particles.

Given quantitative three-dimensional information on the number of Co and Zn atoms throughout the ZIF blend particles, it is then possible to construct two-dimensional histograms to extract information on the mixing processes in these particles. In the two reconstructions it was directly possible to produce a histogram in terms of the number of Co and Zn atoms. However, these are not the physically informative axes. Instead, the relative composition (atomic fraction) was calculated as well as the density at each volume element (voxel). Here the atomic fraction was calculated as X = Zn/(Zn+Co). Figure 6 presents the resulting histograms on these transformed axes. These histograms can now be read as phase diagrams for the composition and density found in the ZIF glass blend particles. The total number density, taken as the sum of Co and Zn number densities, was used to define the particle interior. ESF function fitting was applied, as for the ADF tomogram segmentation for the determination of thickness maps, to determine a threshold for voxels inside the particle. In Figure 6, no intensity is shown in the histogram below this threshold on the basis that composition loses physical meaning when

number densities (and X-ray counts) are low outside the particle. Figure S8 presents the histograms without thresholding.

Figure 6(a) shows two bright regions in the histogram, at the two opposite extremes of the atomic fraction axis. This structure is characteristic of two segregated phases. The densities are similar, with the Co-rich domain (near zero fraction Zn) exhibiting a density of approximately 5 atoms nm^{-3} and the Zn-rich domain exhibiting a density of approximately 6 atoms nm^{-3}. The major fraction of the particle analysed was nearly pure Zn (near one fraction Zn) resulting in the observed saturation near unity fraction Zn at the intensity scaling suitable for visualization of the Co volume. An alternative intensity scaling showing that this saturated region consists of a symmetrically distributed near pure Zn phase is presented in Fig. S9. Although the bulk ratio of a_TZIF-4-Co:a_gZIF-62 is 50:50, this particular particle contained a significantly larger volume of a_gZIF-62, as would be expected within a fragment derived from a domain microstructure. Based on the distribution in measured densities for approximately single-phase regions, the precision in atomic density was estimated at ±2 atoms nm^{-3} (±2 standard deviations, see also Supplementary Material). As such, the measured densities were indistinguishable from the reference densities for Co ZIF-4 and ZIF-62 glasses. The precision in atomic fraction was estimated at ±0.03 (±3%, ±2 standard deviations).

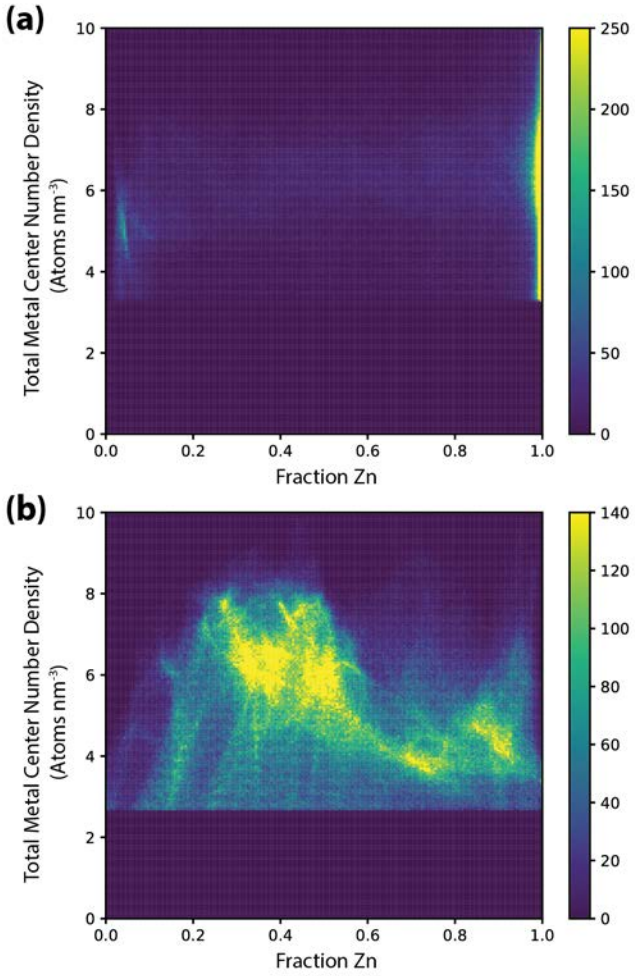

Fig. 6. Two-dimensional histograms for quantitative EDS intensities in the tomographic reconstructions for (a) $(a_T$ZIF-4-Co$)_{0.5}(a_g$ZIF-62$)_{0.5}$ and (b) a_g[(ZIF-67$)_{0.2}$(ZIF-62$)_{0.8}$]. No histogram values (intensities) are shown below the threshold total number density (determined by ESF function fitting) as these voxels were considered outside the particle volume.

While it is conceivably possible that metal centres might move and alter composition during experimental EDS tilt-series acquisition, the $(a_T$ZIF-4-Co$)_{0.5}(a_g$ZIF-62$)_{0.5}$ phase diagram provides a robust control for this possibility, and no significant modification of the segregated phase composition is observed. These observations are consistent with the high viscosity of liquid ZIFs.[34] The flux-melted glass exhibits similar behaviour when not brought to sufficiently high temperatures for flux melting.[6] Consequently, the compositional variations observed by

quantitative EDS tomography at ambient temperature are reasonably attributed only to the mixing during heat treatment in the formation of the glass.

Figure 6(b) presents a more complicated phase diagram for the a_g[(ZIF-67)$_{0.2}$(ZIF-62)$_{0.8}$] flux melted glass. Two major regions were observed in the diagram. First, the Co-rich region is predominantly found to be 0.3-0.5 Zn (30-50% Zn). Second, above 0.55 Zn, the distribution of number densities shifts, forming a distinct Zn-rich region up to and including pure Zn (approaching 1.0 fraction Zn). The density of the mixed Co-rich region is approximately 6 atoms nm^{-3} whereas the lower density Zn-rich region is centered at approximately 4 atoms nm^{-3}. Under the reasonable assumption that errors in the overall method are comparable to those observed in the phase-segregated (a_TZIF-4-Co)$_{0.5}$(a_gZIF-62)$_{0.5}$ blend particle, these densities appear to be distinguishable. These results indicate that there is an upper bound on the Zn content in the Co (ZIF-67) volumes of approximately 55% at which point the Co is found in a distinct Zn-rich phase.

This analysis suggests a mechanistic hypothesis for mixing in a_g[(ZIF-67)$_{0.2}$(ZIF-62)$_{0.8}$], where the ZIF-62 liquid initially migrates into the ZIF-67 structure, giving rise to the higher density mixed phase. Then, the resulting flux-melting of the ZIF-67 leads to diffusion of ZIF-67 back into the external ZIF-62 liquid. Due to the ratio of ZIF-67 and ZIF-62 in the bulk ensemble mixture, domains of phase-pure ZIF-62 remain as well. This suggested mechanism is consistent with reports on the melting of ZIF-62 preceding that of ZIF-8 in the Zn/Zn analogue.[6] The viscosity of the constituent phases and the thermodynamics of mixing associated with the different ligand interactions may play key roles but these quantities are not well characterized, at present, across the limited MOF glass family. The mechanistic insight offered here will inform investigations of the driving forces underlying mixing processes in MOF glasses, which are not yet framed clearly in the still rapidly emerging field of MOF glasses and modelling of liquid phase MOFs.[34]

III. Conclusions

STEM-EDS tomography with absolute quantification has been developed and applied to reveal in detail two distinct mixing processes observed in multicomponent ZIF glasses. A heterogeneous phase-segregated domain structure has been confirmed in $(a_{\mathrm{T}}\text{ZIF-4-Co})_{0.5}(a_{\mathrm{g}}\text{ZIF-62})_{0.5}$ and homogeneous mixing in flux-melted $a_{\mathrm{g}}[(\text{ZIF-67})_{0.2}(\text{ZIF-62})_{0.8}]$ has been revealed. Quantitative nano-tomography has in turn enabled the construction of phase diagrams for these mixtures from nanoscale volumes, providing critical insight into the phases resulting from blending of immiscible and miscible MOFs. These illustrative examples outline directions for further synthetic development and understanding the relationship between the mixing, microstructure, and macroscopic properties of these and other emerging MOF glass materials.

Supplementary Material

See supplementary material for additional experimental details and additional supplementary figures and tables.

Acknowledgments

S.M.C. acknowledges the Henslow Research Fellowship and Girton College, Cambridge. K.E.M. acknowledges the Helmholtz Association for funding this research through a Postdoctoral Research Fellowship. T.D.B. would like to thank the Royal Society for a University Research Fellowship (UF150021), and EPSRC (grant EP/R015481/1). L.L. acknowledges an EPSRC studentship. P.A.M. acknowledges the EPSRC (EP/R008779/1). M.B. acknowledges the Leverhulme Trust Early Career Fellowship ECF-2016-611. C.-B.S. acknowledges support from the Leverhulme Trust project Breaking the non-convexity barrier, EPSRC grant EP/M00483X/1, EPSRC centre EP/N014588/1 and from CHiPS (Horizon 2020 RISE project grant). R.T. acknowledges funding from EPSRC grant EP/L016516/1 for the Cambridge Centre for Analysis. R.T. and C.-B.S. also acknowledge the Cantab Capital Institute for Mathematics of Information.

References

[1] J.E. Shelby, *Introduction to Glass Science and Technology* (2005).

[2] K. Mortensen, W. Brown, and B. Nordén, Phys. Rev. Lett. **68**, 2340 (1992).

[3] M. Chen, NPG Asia Mater. **3**, 82 (2011).

[4] T.D. Bennett and S. Horike, Nat. Rev. Mater. **3**, 431 (2018).

[5] L. Longley, S.M. Collins, C. Zhou, G.J. Smales, S.E. Norman, N.J. Brownbill, C.W. Ashling, P.A. Chater, R. Tovey, C.-B. Schönlieb, T.F. Headen, N.J. Terrill, Y. Yue, A.J. Smith, F. Blanc, D.A. Keen, P.A. Midgley, and T.D. Bennett, Nat. Commun. **9**, 2135 (2018).

[6] L. Longley, S.M. Collins, S. Li, G.J. Smales, I. Erucar, A. Qiao, J. Hou, Cara M. Doherty, A.W. Thornton, A.J. Hill, X. Yu, N.J. Terrill, A.J. Smith, S.M. Cohen, P.A. Midgley, D.A. Keen, S.G. Telfer, and T.D. Bennett, Chem. Sci. **10**, 3592 (2019).

[7] K.S. Park, Z. Ni, A.P. Côté, J.Y. Choi, R. Huang, F.J. Uribe-Romo, H.K. Chae, M. O'Keeffe, and O.M. Yaghi, Proc. Natl. Acad. Sci. **103**, 10186 (2006).

[8] T.D. Bennett, J.-C. Tan, Y. Yue, E. Baxter, C. Ducati, N.J. Terrill, H.H.-M. Yeung, Z. Zhou, W. Chen, S. Henke, A.K. Cheetham, and G.N. Greaves, Nat. Commun. **6**, 8079 (2015).

[9] T.J.A. Slater, A. Macedo, S.L.M. Schroeder, M.G. Burke, P. O'Brien, P.H.C. Camargo, and S.J. Haigh, Nano Lett. **14**, 1921 (2014).

[10] B. Goris, L. Polavarapu, S. Bals, G. Van Tendeloo, and L.M. Liz-Marzán, Nano Lett. **14**, 3220 (2014).

[11] N. Liakakos, C. Gatel, T. Blon, T. Altantzis, S. Lentijo-Mozo, C. Garcia-Marcelot, L.-M. Lacroix, M. Respaud, S. Bals, G. Van Tendeloo, and K. Soulantica, Nano Lett. **14**, 2747 (2014).

[12] D. Rossouw, R. Krakow, Z. Saghi, C.S.M. Yeoh, P. Burdet, R.K. Leary, F. de la Peña, C. Ducati, C.M.F. Rae, and P.A. Midgley, Acta Mater. **107**, 229 (2016).

[13] T.J.A. Slater, R.S. Bradley, G. Bertali, R. Geurts, S.M. Northover, M.G. Burke, S.J. Haigh, T.L. Burnett, and P.J. Withers, Sci. Rep. **7**, 7332 (2017).

[14] G. Haberfehlner, A. Orthacker, M. Albu, J. Li, and G. Kothleitner, Nanoscale **6**, 14563 (2014).

[15] P. Burdet, Z. Saghi, A.N. Filippin, A. Borrás, and P.A. Midgley, Ultramicroscopy **160**, 118 (2016).

[16] G. Cliff and G.W. Lorimer, J. Microsc. **103**, 203 (1975).

[17] M. Watanabe and D.B. Williams, J. Microsc. **221**, 89 (2006).

[18] D. Zanaga, F. Bleichrodt, T. Altantzis, N. Winckelmans, W.J. Palenstijn, J. Sijbers, B. de Nijs, M.A. van Huis, A. Sánchez-Iglesias, L.M. Liz-Marzán, A. van Blaaderen, K. Joost Batenburg, S. Bals, and G. Van Tendeloo, Nanoscale **8**, 292 (2016).

[19] D. Zanaga, T. Altantzis, L. Polavarapu, L.M. Liz-Marzán, B. Freitag, and S. Bals, Part. Part. Syst. Charact. **33**, 396 (2016).

[20] P. Rueda-Fonseca, E. Robin, E. Bellet-Amalric, M. Lopez-Haro, M. Den Hertog, Y. Genuist, R. André, A. Artioli, S. Tatarenko, D. Ferrand, and J. Cibert, Nano Lett. **16**, 1637 (2016).

[21] K.E. MacArthur, T.J.A. Slater, S.J. Haigh, D. Ozkaya, P.D. Nellist, and S. Lozano-Perez, Microsc. Microanal. **22**, 71 (2016).

[22] K.E. MacArthur, T.J.A. Slater, S.J. Haigh, D. Ozkaya, P.D. Nellist, and S. Lozano-Perez, Mater. Sci. Technol. **32**, 248 (2016).

[23] A. Varambhia, L. Jones, A. London, D. Ozkaya, P.D. Nellist, and S. Lozano-Perez, Micron **113**, 69 (2018).

[24] D. Zanaga, T. Altantzis, J. Sanctorum, B. Freitag, and S. Bals, Ultramicroscopy **164**, 11 (2016).

[25] B. Goris, W. Van den Broek, K.J. Batenburg, H. Heidari Mezerji, and S. Bals, Ultramicroscopy **113**, 120 (2012).

[26] R. Leary, Z. Saghi, P.A. Midgley, and D.J. Holland, Ultramicroscopy **131**, 70 (2013).

[27] R.K. Leary, A. Kumar, P.J. Straney, S.M. Collins, S. Yazdi, R.E. Dunin-Borkowski, P.A. Midgley, J.E. Millstone, and E. Ringe, J. Phys. Chem. C **120**, 20843 (2016).

[28] O. Scherzer, Computing **60**, 1 (1998).

[29] K. Papafitsoros and C.B. Schönlieb, J. Math. Imaging Vis. **48**, 308 (2014).

[30] K. Bredies, K. Kunisch, and T. Pock, SIAM J. Imaging Sci. **3**, 492 (2010).

[31] J. Kraxner, M. Schäfer, O. Röschel, G. Kothleitner, G. Haberfehlner, M. Paller, and W. Grogger, Ultramicroscopy **172**, 30 (2017).

[32] C.S. Yeoh, D. Rossouw, Z. Saghi, P. Burdet, R.K. Leary, and P.A. Midgley, Microsc. Microanal. **21**, 759 (2015).

[33] N.J. Zaluzec, Microsc. Microanal. **19**, 1262 (2013).

[34] R. Gaillac, P. Pullumbi, K.A. Beyer, K.W. Chapman, D.A. Keen, T.D. Bennett, and F.-X. Coudert, Nat. Mater. **16**, 1149 (2017).